Fast Multi-Objective Aerodynamic Optimization Using Space-Mapping-Corrected Multi-Fidelity Models and Kriging Interpolation

Leifur Leifsson, Slawomir Koziel, Yonatan Tesfahunegn, and Adrian Bekasiewicz

Abstract The chapter describes a computationally efficient procedure for multi-objective aerodynamic design optimization with multi-fidelity models, corrected using space mapping, and kriging interpolation. The optimization procedure utilizes a multi-objective evolutionary algorithm to generate an initial Pareto front which is subsequently refined iteratively using local enhancements of the kriging-based surrogate model. The refinements are realized with space mapping response correction based on a limited number of high-fidelity training points allocated along the initial Pareto front. The method yields—at a low computational cost—a set of designs representing trade-offs between the conflicting objectives. We demonstrate the approach using examples of airfoil design, one in transonic flow and another one in low-speed flow, in low-dimensional design spaces.

Keywords Multi-objective optimization • Aerodynamic design • Multi-fidelity CFD models • Space mapping • Kriging interpolation

MSC code: 65K10

1   Introduction

Aerodynamic design problems are mostly solved using single-objective optimization. However, aerodynamic design is by nature a multi-objective task. Handling the problem as a multi-objective one is often impractical due to the cost of

L. Leifsson (✉)
Department of Aerospace Engineering, Iowa State University, Ames, IA 50011, USA
e-mail: leifur@iastate.edu

S. Koziel • Y. Tesfahunegn • A. Bekasiewicz
Engineering Optimization & Modeling Center, School of Science and Engineering,
Reykjavik University, Menntavegur 1, 101 Reykjavik, Iceland
e-mail: koziel@ru.is; yonatant@ru.is; bekasiewicz@ru.is

running high-fidelity computational fluid dynamics (CFD) simulations, which are ubiquitous in aerodynamic design [1, 2]. Although CFD-based parameter sweeps and engineering experience are common practice when searching for better designs in a single-objective sense, automation using numerical optimization techniques is becoming increasingly popular and necessary [3–6]. A multitude of methods for single-objective optimization problems are available such as conventional gradient-based algorithms [7] (including those utilizing inexpensive adjoint sensitivities [8, 9]), and surrogate-based optimization (SBO) techniques [10–15] that offer efficient global optimization as well as a substantial reduction of the design cost when compared to the traditional methods [12]. In this chapter, we describe an efficient approach to solve multi-objective aerodynamic design problems using high-fidelity simulations and surrogate-based methods.

A Pareto front is a common way of representing solutions to multi-objective problems. It contains a set of the best possible designs which are non-commensurable in the conventional (single-objective sense) [16]. The most widely used multi-objective optimization methods include multi-objective evolutionary algorithms (MOEAs) [17–20]. The computational complexity of MOEAs is high due to the fact that a (usually large) set of designs is being processed in each iteration of the algorithm. SBO [10–15] can be used to reduce the computational cost of multi-objective aerodynamic design by using inexpensive/less costly surrogate functions in lieu of the CPU-intensive high-fidelity models.

In general, the surrogate models can be created by either approximating the sampled high-fidelity model data using regression (so-called data-driven surrogates [10, 11, 15]), or by correcting physics-based low-fidelity models (so-called multi-fidelity surrogates [12–14, 21–23]) which are less accurate but computationally inexpensive/less costly representations of the high-fidelity models.

Data-driven surrogate models can be constructed using polynomial regression, radial basis function interpolation, kriging, and support vector regression [10, 11]. Typically, a substantial amount of data samples, selected using Design of Experiments [11], are required.

Multi-fidelity surrogates [12] are constructed using low-fidelity models that are manipulated to become a reliable representation of the high-fidelity models. The two main parts in constructing a multi-fidelity surrogate are (1) developing the low-fidelity models, and (2) modifying them to achieve a better representation of the high-fidelity models. Techniques to modify (also called correct) the low-fidelity models include bridge functions [24–26], calibration [21, 22], space mapping [27–29, 41], shape-preserving response prediction [30, 31], adaptive response correction [32], and adaptive response prediction [33]. The multi-fidelity models are usually more expensive to evaluate than the data-driven surrogates, but fewer high-fidelity model data are required to obtain a given accuracy level as compared to when using the high-fidelity data in the data-driven surrogates directly.

This chapter describes a multi-objective procedure for aerodynamic design exploiting low-fidelity CFD simulations, space mapping, kriging interpolation, and MOEAs. The procedure is illustrated using examples involving the design of transonic and low-speed airfoil shapes.

2 Methodology

In this section, we provide a formulation of the multi-objective design problem, a procedure for constructing multi-fidelity surrogate model, as well as outline the multi-objective optimization algorithm.

2.1 Problem Formulation

Let x be an $n \times 1$ vector of the design variables, and $f(x) = [f_1(x)\, f_2(x)\, \dots\, f_q(x)]^T$ be a $q \times 1$ vector of the high-fidelity model responses. Examples of responses include the airfoil section drag coefficient $f_1(x) = C_{d.f}$ and the section lift coefficient $f_2(x) = C_{l.f}$. Let $F_{obj,i}(x)$, $i = 1, \dots, N_{obj}$, be the ith design objective. A typical performance objective would be to minimize the drag coefficient, in which case $F_{obj,i}(x) = C_{d.f}$. Another objective would be to maximize lift, in which case $F_{obj,i}(x) = 1/C_{l.f}$ or $F_{obj,i}(x) = -C_{l.f}$ (normally, the objectives are supposed to be minimized so the maximization problem has to be transformed into a minimization one before carrying out the design process). Yet another objective could be to minimize a noise metric NM_f, in which case $F_{obj,i}(x) = NM_f$.

If $N_{obj} > 1$, then any two designs $x^{(1)}$ and $x^{(2)}$ for which $F_{obj,i}(x^{(1)}) < F_{obj,i}(x^{(2)})$ and $F_{obj,l}(x^{(2)}) < F_{obj,l}(x^{(1)})$ for at least one pair $i \neq l$, are not commensurable, i.e., none is better than the other in the multi-objective sense. We define Pareto-dominance relation Υ (see, e.g., Fonseca [16]), saying that for the two designs x and y, we have $x \,\Upsilon\, y$ (x dominates over y) if $F_{obj,i}(x) \leq F_{obj,i}(y)$ for all $i = 1, \dots, N_{obj}$, and $F_{obj,i}(x) < F_{obj,i}(y)$ for at least one i. In other words, the point x dominates over y if it is not worse than y with respect to all objectives, and it is better than y with respect to at least one objective. The goal of the multi-objective optimization is to find a representation of a Pareto front X_P of the design space X, such that for any $x \in X_P$, there is no $y \in X$ for which $y \,\Upsilon\, x$ (Fonseca [16]).

2.2 Multi-Fidelity Surrogate Model Construction

The process of finding the Pareto front is realized using evolutionary algorithms (EAs) [17]. EAs iteratively process the entire set of potential solutions to the problem at hand. Therefore, they typically require numerous evaluations of the objective function. Consequently, using the expensive high-fidelity model, $f(x)$, directly in the multi-objective optimization is normally prohibitive. This difficulty is alleviated using a surrogate model, $s(x)$, constructed using a corrected low-fidelity model, $c(x)$.

A low-fidelity model can be developed based on, for example, (1) simplified physics, (2) reduced grid discretization, and (3) reduced solver convergence criteria, or any combination of the aforementioned approaches [13]. Here, we use a combination of approaches (2) and (3).

Given the low-fidelity model $c(x)$ the process of constructing the surrogate is as follows. Let $c(x) = [c_1(x) \; c_2(x) \; \ldots \; c_q(x)]^T$ denote a $q \times 1$ vector of responses from the low-fidelity model. We will use a response with $q = 3$, and $c_1(x) = C_{l.c}(x)$, $c_2(x) = C_{d.c}(x)$, and $c_3(x) = NM_c(x)$ to demonstrate the construction process (here, $C_{l.c}$ and $C_{d.c}$ are the lift and drag coefficients, respectively, and NM_c is the noise metric). The surrogate model is constructed in two steps.

In Step 1, the multi-point space mapping correction is applied to the low-fidelity model. The initial surrogate model $s_0(x)$, a vector of the same dimension as $c(x)$, is obtained by applying a parameterized output space mapping [27, 28, 34]. The mapping uses the correction terms that are directly applied to the response components $C_{l.c}(x)$, $C_{d.c}(x)$, and $NM_c(x)$ of the low-fidelity model. The initial surrogate model is defined as [27]

$$
s_0(x) = A(x) \circ c(x) + D(x) = \Big[a_l(x) C_{l.c}(x) + d_l(x) \quad a_d(x) C_{d.c}(x) + \\
+ d_d(x) \quad a_N(x) NM_c(x) + d_N(x) \Big]^T, \tag{1}
$$

where $\circ$ denotes component-wise multiplication. Both the multiplicative and additive correction terms are design-variable-dependent and take the form of

$$
A(x) = \Big[a_{l.0} + [a_{l.1} \; a_{l.2} \; \ldots \; a_{l.n}] \cdot (x - x^0) \quad a_{d.0} + [a_{d.1} \; a_{d.2} \; \ldots \; a_{d.n}] \cdot (x - x^0) \\
a_{N.0} + [a_{N.1} \; a_{N.2} \; \ldots \; a_{N.n}] \cdot (x - x^0) \Big]^T, \tag{2}
$$

$$
D(x) = \Big[d_{l.0} + [d_{l.1} \; d_{l.2} \; \ldots \; d_{l.n}] \cdot (x - x^0) \quad d_{d.0} + [d_{d.1} \; d_{d.2} \; \ldots \; d_{d.n}] \cdot (x - x^0) \\
d_{N.0} + [d_{N.1} \; d_{N.2} \; \ldots \; d_{N.n}] \cdot (x - x^0) \Big]^T, \tag{3}
$$

where x^0 is the center of the design space. The response correction parameters A and D are obtained as

$$
[A, D] = \arg \min_{[A, D]} \sum_{k=1}^{N} || f(x^k) - (\overline{A}(x^k) \circ c(x^k) + \overline{D}(x^k)) ||^2, \tag{4}
$$

i.e., the response scaling is supposed to (globally) improve the matching for all training points x^k, $k = 1, \ldots, N$, where N is the number of training points.

A training set combining the following subsets is used: (1) a star-distribution design of experiments with $N = 2n + 1$ training points (n being the number of design variables) allocated at the center of the design space $x^0 = (l + u)/2$ (l and u being the

lower and upper bound for the design variables, respectively), and the centers of its faces, i.e., points with all coordinates but one equal to those of x^0, and the remaining one equal to the corresponding component of l or u; this sampling scheme is also referred to as the star distribution [12], (2) design space corners, and (3) additional points allocated using the Latin Hypercube Sampling (LHS) [40]. In the application examples given in Sections 3 and 4 of this chapter, we use all three subsets (with $N = 10$ LHS points) for transonic airfoil design, and only (1) and (3) for low-speed airfoil design.

The problem (4) is equivalent to the linear regression problems $C_l[a_{l.0} \, a_{l.1} \, \dots \, a_{l.n} \, d_{l.0} \, d_{l.1} \, \dots \, d_{l.n}]^T = F_l$, $C_d[a_{d.0} \, a_{d.1} \, \dots \, a_{d.n} \, d_{d.0} \, d_{d.1} \, \dots \, d_{d.n}]^T = F_d$, and $C_N[a_{N.0} \, a_{N.1} \, \dots \, a_{N.n} \, d_{N.0} \, d_{N.1} \, \dots \, d_{N.n}]^T = F_N$, where the matrices C_l, C_d, C_N, F_l, F_d, and F_N are defined as

$$C_l = \begin{bmatrix} C_{l.c}(x^1) & C_{l.c}(x^1) \cdot (x_1^1 - x_1^0) & \cdots & C_{l.c}(x^1) \cdot (x_n^1 - x_n^0) & 1 & (x_1^1 - x_1^0) & \cdots & (x_n^1 - x_n^0) \\ C_{l.c}(x^2) & C_{l.c}(x^2) \cdot (x_1^2 - x_1^0) & \cdots & C_{l.c}(x^2) \cdot (x_n^2 - x_n^0) & 1 & (x_1^1 - x_1^1) & \cdots & (x_n^1 - x_n^0) \\ \vdots & \vdots & \ddots & \vdots & \vdots & \vdots & \vdots & \vdots \\ C_{l.c}(x^N) & C_{l.c}(x^N) \cdot (x_1^N - x_1^0) & \cdots & C_{l.c}(x^N) \cdot (x_n^N - x_n^0) & 1 & (x_1^1 - x_1^1) & \cdots & (x_n^1 - x_n^0) \end{bmatrix}$$
(5)

$$F_l = \begin{bmatrix} C_{l.f}(x^1) & C_{l.f}(x^2) & \dots & C_{l.f}(x^N) \end{bmatrix}^T$$
(6)

$$C_d = \begin{bmatrix} C_{d.c}(x^1) & C_{d.c}(x^1) \cdot (x_1^1 - x_1^0) & \cdots & C_{d.c}(x^1) \cdot (x_n^1 - x_n^0) & 1 & (x_1^1 - x_1^0) & \cdots & (x_n^1 - x_n^0) \\ C_{d.c}(x^2) & C_{d.c}(x^2) \cdot (x_1^2 - x_1^0) & \cdots & C_{d.c}(x^2) \cdot (x_n^2 - x_n^0) & 1 & (x_1^1 - x_1^0) & \cdots & (x_n^1 - x_n^0) \\ \vdots & \vdots & \ddots & \vdots & \vdots & \vdots & \vdots & \vdots \\ C_{d.c}(x^N) & C_{d.c}(x^N) \cdot (x_1^N - x_1^0) & \cdots & C_{d.c}(x^N) \cdot (x_n^N - x_n^0) & 1 & (x_1^1 - x_1^0) & \cdots & (x_n^1 - x_n^0) \end{bmatrix}$$
(7)

$$F_d = \begin{bmatrix} C_{d.f}(x^1) & C_{d.f}(x^2) & \dots & C_{d.f}(x^N) \end{bmatrix}^T$$
(8)

$$C_N = \begin{bmatrix} NM_c(x^1) & NM_c(x^1) \cdot (x_1^1 - x_1^0) & \cdots & NM_c(x^1) \cdot (x_n^1 - x_n^0) & 1 & (x_1^1 - x_1^0) & \cdots & (x_n^1 - x_n^0) \\ NM_c(x^2) & NM_c(x^2) \cdot (x_1^2 - x_1^0) & \cdots & NM_c(x^2) \cdot (x_n^2 - x_n^0) & 1 & (x_1^1 - x_1^0) & \cdots & (x_n^1 - x_n^0) \\ \vdots & \vdots & \ddots & \vdots & \vdots & \vdots & \vdots & \vdots \\ NM_c(x^N) & NM_c(x^N) \cdot (x_1^N - x_1^0) & \cdots & NM_c(x^N) \cdot (x_n^N - x_n^0) & 1 & (x_1^1 - x_1^0) & \cdots & (x_n^1 - x_n^0) \end{bmatrix}$$
(9)

$$F_N = \begin{bmatrix} NM_f(x^1) & NM_f(x^2) & \dots & NM_f(x^N) \end{bmatrix}^T$$
(10)

The dimension of the vectors F_l, F_d, and F_N is $N \times 1$, and the dimension of the matrices C_l, C_d, and C_N is $N \times 2(n+1)$. The correction matrices A and D can now be found analytically as a least-square optimal solution to the aforementioned regression problems

$$
\begin{bmatrix} a_{l.0} \\ a_{l.1} \\ \vdots \\ a_{l.n} \\ d_{l.0} \\ \vdots \\ d_{l.n} \end{bmatrix} = \left(C_l^T C_l \right)^{-1} C_l^T F_l, \quad
\begin{bmatrix} a_{d.0} \\ a_{d.1} \\ \vdots \\ a_{d.n} \\ d_{d.0} \\ \vdots \\ d_{d.n} \end{bmatrix} = \left(C_d^T C_d \right)^{-1} C_d^T F_d, \quad
\begin{bmatrix} a_{N.0} \\ a_{N.1} \\ \vdots \\ a_{N.n} \\ d_{N.0} \\ \vdots \\ d_{N.n} \end{bmatrix} = \left(C_N^T C_N \right)^{-1} C_N^T F_N
$$

$$(11)$$

Note that the matrices $C_l^T C_l$, $C_d^T C_d$, and $C_N^T C_N$ are non-singular for $N > n + 1$, which is the case for our choice of the training set.

In Step 2, we construct the kriging surrogate model. Having the space-mapping-corrected low-fidelity model from Step 1, we sample the initial surrogate and create the kriging interpolation model of it [10, 11]. The kriging surrogate model, s, is very fast, smooth, and easy to optimize. In particular, a large number of model evaluations can be done at low cost in the context of multi-objective optimization using evolutionary methods. Step 1 of the surrogate modeling process allows us to reduce misalignment between the low- and high-fidelity models. The surrogate model created in Step 2 is a data-driven model so that it is fast and yet accurate because relatively dense sampling of the design space is utilized. Nevertheless, the computational cost of the surrogate is reasonably low because it is based on low-fidelity model data.

2.3 Optimization Method

The multi-objective design optimization flow can be summarized as follows:

1. Correct the low-fidelity model c using parameterized output space mapping as in Eqn. (1), in particular, identify the correction matrices $A(x)$ and $D(x)$;
2. Sample the design space and acquire the s_0 data (i.e., evaluate the low-fidelity model c at the selected locations and apply the correction in Eqn. (1) using $A(x)$ and $D(x)$ from Step 1);
3. Construct the kriging interpolation surrogate model s using the sample values obtained in Step 2;
4. Obtain the Pareto front by optimizing s using MOEA;
5. Evaluate high-fidelity model at selected geometries from the Pareto front.
6. If the termination condition is not satisfied, add the new high-fidelity data set to the existing one, and go to Step 1.
7. END

The first four steps of the method lead to obtaining an initial representation of the Pareto front by optimizing the surrogate model s in a multi-objective sense using

a multi-objective evolutionary algorithm (MOEA). In the illustration examples in Sections 3 and 4, we use a standard multi-objective evolutionary algorithm with fitness sharing, Pareto-dominance tournament selection, and mating restrictions [16, 17].

The surrogate model is updated upon conclusion of the verification stage (Step 5) by executing the output space mapping procedure using the entire high-fidelity model data set (the original one and the Pareto front representation). The geometries in Step 5 are selected uniformly along the Pareto front. The number of selected geometries is not critical, in the illustration examples, we use around 10 samples per iteration. The improved surrogate model is then re-optimized in a multi-objective sense.

The computational cost of each iteration of the above procedure is only due to the evaluation of the high-fidelity model at the geometries picked up from the Pareto front (in practice, a few points are sufficient). Moreover, the design space in the refinement iterations can be restricted to only the part that contains the Pareto set (the remaining part of the space is irrelevant) to reduce the number of required evaluations. The termination condition is based on comparison between the Pareto front produced by optimizing the current surrogate model and the high-fidelity verification samples.

3 Example 1: Transonic Airfoil Design

The first test case considers the design of airfoils in transonic flow involving lift and drag as design objectives.

3.1 *Problem Formulation*

A specific case of transonic airfoil shape design with the aim at maximizing the section lift coefficient and minimizing the section drag coefficient at the same time is considered. In other words, we have two objectives, $F_{obj,1}(\boldsymbol{x}) = 1/C_{l,f}$ and $F_{obj,2}(\boldsymbol{x}) = C_{d,f}$. We fix the operating conditions at a free-stream Mach number of $M_{\infty} = 0.75$ and an angle of attack of $\alpha = 1$ deg. The airfoil shapes are parameterized by the NACA four-digit parameterization [35], where the airfoil shape design variables are m (the maximum ordinate of the mean camber line as a fraction of chord), p (the chordwise position of the maximum ordinate), and t/c (the maximum thickness-to-chord ratio). The design variable vector is $\boldsymbol{x} = [m \; p \; t/c]^{T}$.

The airfoils are constructed by combining a thickness function $z_t(x/c)$ with a mean camber line function $z_c(x/c)$. The x/c- and z/c-coordinates are [35]

$$(x/c)_{u,l} = (x/c) \mp (z_t/c) \, \sin \theta, \; (z/c)_{u,l} = (z_c/c) \pm (z_t/c) \, \cos \theta, \qquad (12)$$

where u and l refer to the upper and lower surfaces, respectively, and

$$\theta = \tan^{-1}\left(\frac{d\,(z_c/c)}{d\,(x/c)}\right), \tag{13}$$

is the mean camber line slope. The NACA four-digit thickness distribution is given by

$$(z_t/c) = t\left(a_0(x/c)^{1/2} - a_1\,(x/c) - a_2(x/c)^2 + a_3(x/c)^3 - a_4(x/c)^4\right), \tag{14}$$

where $a_0 = 1.4845$, $a_1 = 0.6300$, $a_2 = 1.7580$, $a_3 = 1.4215$, $a_4 = 0.5075$, and t is the maximum thickness. We use the following parameter bounds: $0.0 \leq m \leq 0.03$, $0.2 \leq p \leq 0.8$, and $0.08 \leq t \leq 0.14$. There is one nonlinear constraint regarding the cross-section area A (non-dimensionalized by the chord squared), i.e., $A \geq 0.075$.

3.2 High-Fidelity Model

The flow is assumed to be steady, inviscid, and adiabatic with no body forces. The compressible Euler equations are taken to be the governing fluid flow equations. The solution domain boundaries are placed at 25 chord lengths in front of the airfoil, 50 chord lengths behind it, and 25 chord lengths above and below it, see Fig. 1a. The computational meshes are of structured curvilinear body-fitted C-topology with elements clustering around the airfoil and growing in size with distance from the airfoil surface. The computer code ICEM CFD [29] is used for the mesh generation. An example mesh is shown in Fig. 1b.

The free-stream Mach number, static pressure, and angle of attack are prescribed at the farfield boundary. The flow solver is of implicit density-based formulation and the inviscid fluxes are calculated by an upwind-biased second-order spatially
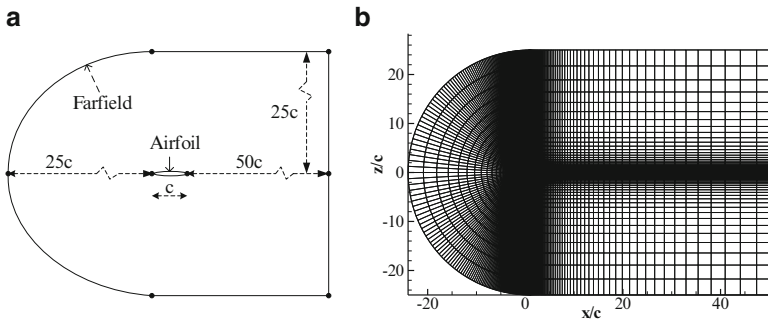
**Fig. 1** Elements of the computational mesh: (**a**) sketch of the computational domain, (**b**) an example mesh
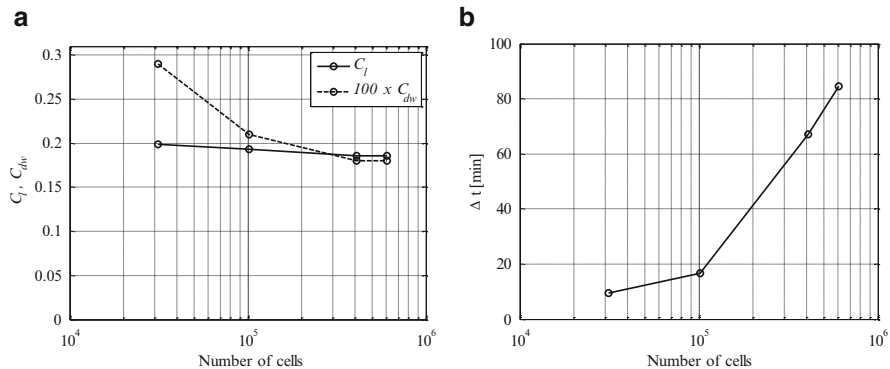
Fig. 2 Grid convergence study using the NACA 0012 airfoil at a Mach number of $M_\infty = 0.75$ and an angle of attack of $\alpha = 1°$: (**a**) the lift and drag coefficients versus the number mesh cells, and (**b**) the simulation time versus the number of mesh cells

accurate Roe flux scheme. Asymptotic convergence to a steady-state solution is obtained for each case. The solution convergence criterion for the high-fidelity model is the one that occurs first of the following: a reduction of all the residuals by six orders, or a maximum number of iterations of 1000. Numerical fluid flow simulations are performed using the computer code FLUENT [29].

A grid convergence study was performed using the NACA 0012 airfoil at a Mach number of $M_\infty = 0.75$ and an angle of attack of $\alpha = 1°$. The study, shown in Fig. 2a, revealed that roughly 400,000 mesh cells are needed for mesh convergence, and that particular mesh was used for the high-fidelity model. The overall simulation time for the case considered is around 67 min (Fig. 2b) using four processors on an Intel (R) Xeon CPU E5-2620@2.00 GHz machine. The flow solver reached a converged solution after 352 iterations. The other meshes required around 350–500 iterations to converge, except the coarsest mesh, which terminated after 1000 iterations, with the overall simulation time around 9.5 min on the same four processors as the high-fidelity model.

3.3 Low-Fidelity Model

The low-fidelity CFD model is constructed in the same way as the high-fidelity model, but with a coarser computational mesh and relaxed convergence criteria. For the low-fidelity model, we use the coarse mesh in the grid study presented in Fig. 3a, with roughly 30,000 mesh cells. The flow solution history for the low-fidelity model, shown in Fig. 3a, indicates that the lift and drag coefficients are nearly converged after 80–100 iterations. The maximum number of iterations is set to 100 for the low-fidelity model. This reduced the overall simulation time to 1.5 min. A comparison of the pressure distributions, shown in Fig. 3b, indicates that the low-fidelity model,
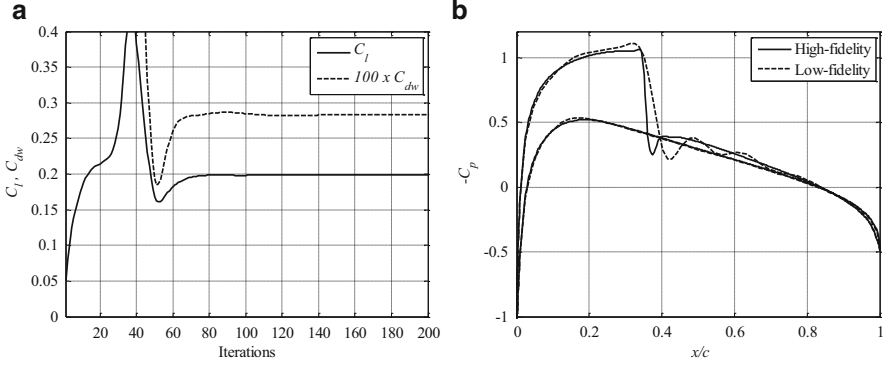
Fig. 3 Simulation results for NACA 0012 at a Mach number of $M_\infty = 0.75$ and an angle of attack of $\alpha = 1°$: (**a**) the evolution of the lift and drag coefficients obtained by the low-fidelity model; (**b**) a comparison of the pressure distributions obtained by the high- and low-fidelity models

in spite of being based on much coarser mesh and reduced flow solver iterations, captures the main features of the high-fidelity model pressure distribution quite well. The biggest discrepancy in the distributions is around the shock on the upper surface, leading to an over estimation of both lift and drag (Fig. 3a).

The ratio of the simulation times of the high- and low-fidelity model in this case study is 43.8. In many cases the solver does not fully converge with respect to the residuals and goes on up to 1000 iterations. Then the overall evaluation time of the high-fidelity model goes up to 170 min. In those cases, the ratio of the simulation times of the high- and low-fidelity models is around 110. For the sake of simplicity, we will use a fixed value of 80 in the numerical computations presented in the results section.

3.4 Results

The Pareto set obtained in the first iteration is shown in Fig. 4a. It is generated by optimizing the initial kriging model, i.e., the one constructed from the space-mapping-corrected low-fidelity model (Eqns. (1)–(11), but without the noise metric values) with the training samples allocated as described below Eqn. (4). The new set of ten high-fidelity samples allocated along that initial Pareto front representation (only nine of them are shown in Fig. 4a) is used for verification purposes but also to enhance the surrogate model by re-running the space mapping corrections (Eqns. (1)–(11)). It can be observed that there is some discrepancy between the Pareto-optimized surrogate model and the sampled high-fidelity model, which means that the optimization process has to be continued. The final Pareto set shown in Fig. 4b is obtained after four iterations of the algorithm. Its verification carried out using an additional set of high-fidelity model samples indicates that the surrogate model
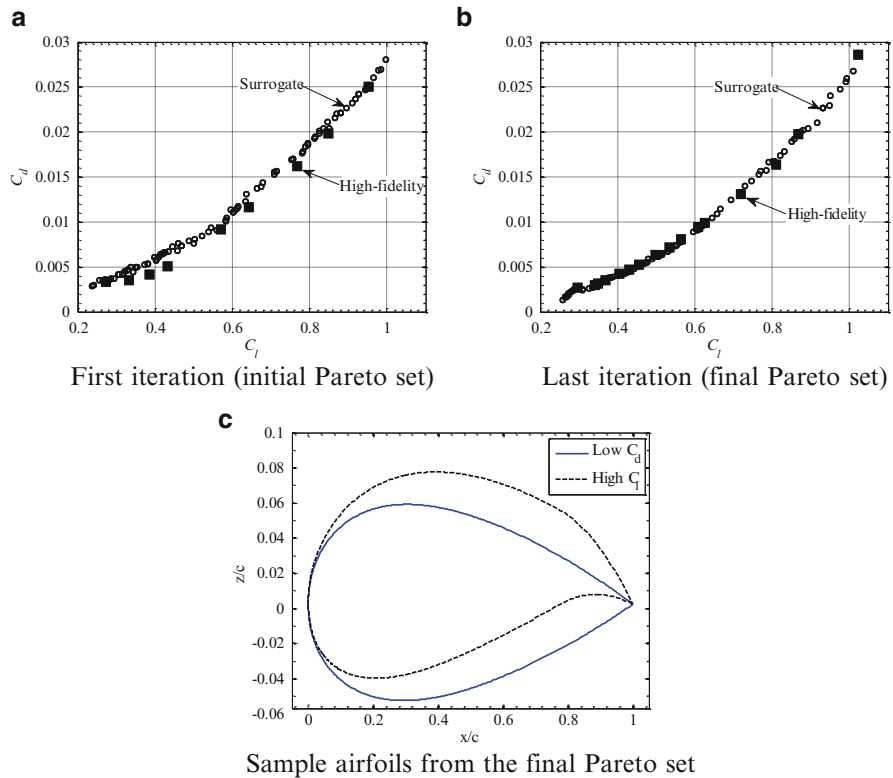
Fig. 4 Pareto front representation obtained by optimizing the surrogate model: (**a**) and (**b**) show the surrogate model points (*circles*), and selected high-fidelity model points (*squares*), and (**c**) shows airfoil shapes from the final Pareto set (**b**) for low drag coefficient and high lift coefficient

is a sufficiently good representation of the high-fidelity model (both data set are practically aligned). The total optimization cost is about 60 high-fidelity model evaluations: 30 to obtain the initial set as mentioned above, and ten per each additional iteration of the algorithm.

Figure 4c shows the airfoil shapes from the final Pareto set (Fig. 4b) with a low drag coefficient ($x = [0.0013\ 0.5326\ 0.1117]^T$), i.e., the left-most high-fidelity sample on Fig. 4b, and a high lift coefficient ($x = [0.0267\ 0.7725\ 0.1134]^T$), i.e., the right-most high-fidelity sample on Fig. 4b. Both designs fulfill the cross-sectional area constraint, i.e., $A_{low\ Cd} \geq 0.075$ and $A_{high\ Cl} \geq 0.075$. The two airfoil shapes have similar thickness ($t_{low\ Cd} \approx t_{high\ Cl} \approx 0.11$), but the design with lower drag has a much lower camber than the one with higher lift ($m_{low\ Cd} = 0.0013$ vs. $m_{high\ Cl} = 0.0267$).

4 Example 2: Low-Speed Airfoil Design

The second test case involves low-speed airfoil design with trade-offs of aerodynamic performance versus noise signature.

4.1 Problem Formulation

This example involves the trade-off between the aerodynamic and aeroacoustic performances of low-speed airfoils. We consider only the clean wing, trailing-edge (TE) noise in this example, and we aim at minimizing the section drag coefficient ($C_{d,f}$) for a given section lift coefficient ($C_{l,f}$), and at the same time minimize the TE noise (given by a noise metric NM_f explained in the next section). Therefore, we have two objectives, $F_{obj,1}(\boldsymbol{x}) = C_{d,f}$ and $F_{obj,2}(\boldsymbol{x}) = NM_f$, both obtained by a high-fidelity simulation.

The specific design case considered is optimization for a target lift coefficient of $C_l = 1.5$. The operating conditions are a free-stream Mach number of $M_\infty = 0.208$ and a Reynolds number of $Re_c = 0.665$ million. The angle of attack α is a dependent variable utilized to obtain, for any given airfoil geometry, the target lift coefficient. We use again the NACA four-digit parameterization [35] (as described in Section III.A.1) with the following parameter bounds: $0.0 \leq m \leq 0.1$, $0.3 \leq p \leq 0.6$, and $0.08 \leq t \leq 0.14$. There are no other constraints considered in the optimization process.

The kriging surrogate model constructed for the purpose of evolutionary-based multi-objective optimization was obtained using 343 low-fidelity model samples allocated on a uniform rectangular $7 \times 7 \times 7$ grid. The surrogate was further corrected using the multi-point output space mapping (1), and utilizing nine high-fidelity model samples: seven samples allocated according to the star-distribution factorial design of experiments, and two additional random samples necessary to ensure that the regression problem has a unique solution.

4.2 Noise Metric Model

The noise metric model was developed by Hosder et al. [36] to give an accurate relative noise measure suitable for design studies. The noise metric therefore does not give an accurate prediction of the absolute noise level. However, it does give an accurate measure of the change in noise due to changes in the wing shape. The noise metric model is recalled here for convenience. A rigorous derivation of the noise metric can be found in Hosder et al. [36].

Fig. 5 Geometrical definition of the noise source, receiver, and directivity angles (note that the trailing-edge sweep angle β is $0°$ here) [36]
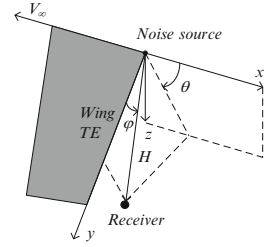
The objective is to estimate the acoustic noise perceived by an observer at a distance H from a clean wing (Fig. 5). An intensity indicator for the clean wing turbulent trailing-edge noise is defined as [36]

$$I_{NM} = \frac{\rho_\infty}{2\pi^3 a_\infty^2} \int_0^{b/2} u_0^5 l_0 \, \mathrm{c} \, os^3\beta \frac{D\left(\theta,\phi\right)}{H^2} dy, \tag{15}$$

where b is the wing span, ρ_∞ is the free-stream density, a_∞ is the free-stream speed of sound, u_0 is the characteristic velocity scale for turbulence, l_0 is the characteristic length scale for turbulence, and β is the trailing-edge sweep angle. $D(\theta,\varphi)$ is the directivity term and is defined as

$$D\left(\theta,\phi\right) = 2\sin^2\left(\frac{\theta}{2}\right)\sin\phi, \tag{16}$$

where θ is the polar directivity angle, and φ is the azimuthal directivity angle (Fig. 5).

The characteristic turbulent velocity at a spanwise location of the wing trailing edge is chosen as the maximum value of the turbulent kinetic energy (*TKE*) profile at that particular spanwise station, that is

$$u_0(y) = \max\left[\sqrt{TKE(z)}\right], \tag{17}$$

where z is the direction normal to the wing surface. The characteristic turbulence length scale at each spanwise station is modeled as

$$l_0(y) = \frac{u_0(y)}{\omega}, \tag{18}$$

where ω is the turbulent frequency (dissipation rate per unit kinetic energy) observed at the maximum *TKE* location.

The noise metric (*NM*) for the trailing-edge noise (in dB) is written as

$$NM = 120 + 10\log\left(I_{NM}\right), \tag{19}$$

where the noise intensity indicator has been scaled with the reference noise intensity of $10^{-12} \, W/m^2$ (the minimum sound intensity level that the human ear can detect). The total noise metric is

$$NM = 10 \log \left(10^{\frac{NM_u}{10}} + 10^{\frac{NM_l}{10}} \right), \tag{20}$$

where NM_u and NM_l are noise metric values obtained by Eqn. (19), evaluated for the upper and lower surfaces, respectively.

4.3 High-Fidelity CFD Model

The flow is assumed to be steady, compressible, and viscous. The steady Reynolds-averaged Navier–Stokes equations are taken as the governing fluid flow equations with the k-ω SST turbulence model by Menter [37]. The solution domain boundaries are placed at 25 chord lengths in front of the airfoil, 50 chord lengths behind it, and 25 chord lengths above and below it. The computational meshes are of structured curvilinear body-fitted C-topology with elements clustering around the airfoil and growing in size with distance from the airfoil surface. The grids are generated using the hyperbolic C-mesh of Kinsey and Barth [38]. The high-fidelity models grid has around 400,000 mesh cells.

Numerical fluid flow simulations are performed using the computer code FLU-ENT [39]. The flow solver is of implicit density-based formulation and the fluxes are calculated by an upwind-biased second-order spatially accurate Roe flux scheme. Asymptotic convergence to a steady-state solution is obtained for each case. The solution convergence criterion for the high-fidelity model is the one that occurs first of the following: a reduction of the residuals by six orders of magnitude, or a maximum number of iterations of 4000.

4.4 Low-Fidelity CFD Model

The low-fidelity CFD model is constructed in the same way as the high-fidelity model, but with a coarser computational mesh and relaxed convergence criteria. The low-fidelity mesh has around 30,000 mesh cells. Although the flow equation residuals are not converged, the lift and drag coefficients and the noise metric typically converge within 1200 iterations. Therefore, the maximum number of iterations is set to 1200.

4.5 Results

Figure 6 shows the distribution of the solutions in the feature (output) space at the first iteration of the evolutionary algorithm. The population size used was $N = 500$.
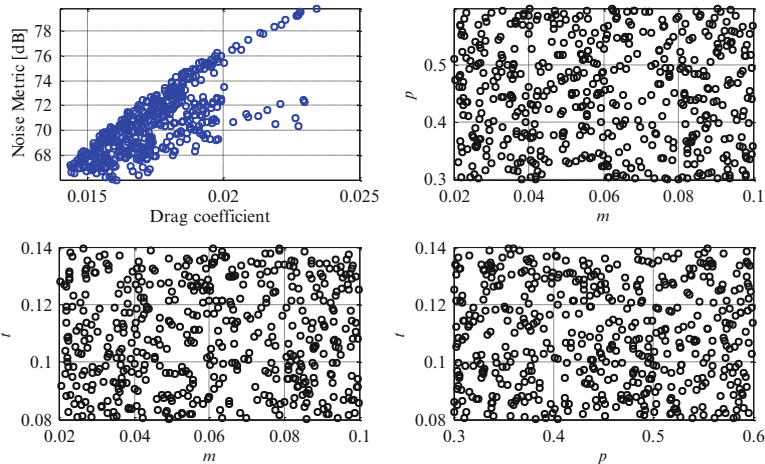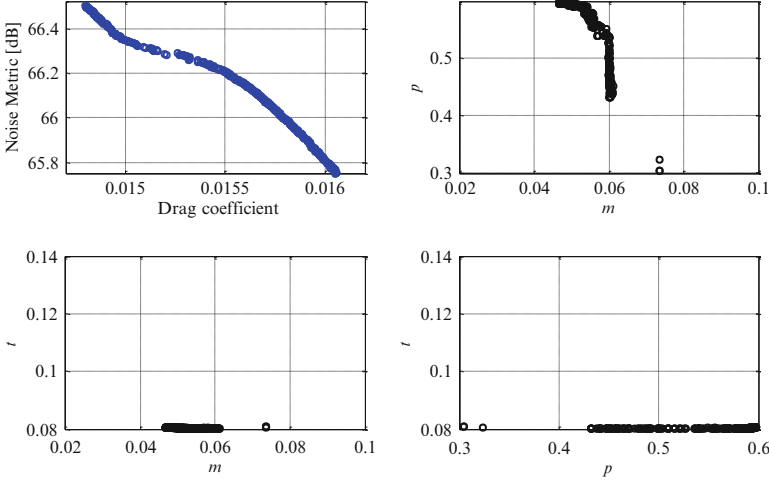
Fig. 6 Multi-objective optimization of the surrogate model: distribution of the initial population in the feature (output) space and the design space

Random initialization with uniform probability distribution is utilized. One can observe a strong correlation between the drag coefficient and the noise metric in the majority of the feature space. Moreover, one can also observe that in a small region of the feature space the two objectives are weakly conflicting, i.e., in the region with low values of both objectives.

The Pareto set obtained after optimizing the surrogate model is shown in Fig. 7, together with the allocation of the solution in the design space. Note that all the Pareto-optimal solutions correspond to the thinnest possible airfoil shapes (here, $t = 0.08$). As there are no thickness constraints, the optimizer reaches the lower bound on the thickness parameter to reduce drag, in particular skin friction drag, while still maintaining the prescribed lift.

Figure 8a shows the high-fidelity model verification samples, indicating certain discrepancies between the drag/noise figures predicted by the surrogate model and actual values. The Pareto front refinement has been subsequently executed in the refined design space of $0.045 \leq m \leq 0.075$, $0.3 \leq p \leq 0.6$, and $0.08 \leq t \leq 0.14$. The verification samples obtained in the previous step have been utilized to update the surrogate model.

The results of the refinement iteration are shown in Fig. 8b. The overall optimization procedure is terminated at this point because the assumed accuracy of <1 drag count (where a drag count is defined to be $\Delta C_d = 0.0001$) and <0.1 dB with respect to the noise metric is met. The final Pareto front shows that the range of the drag coefficients for the trade-off solutions is from 148 to 156 drag counts with the corresponding noise metric from 66.4 dB to 65.6 dB. Thus, improvement of the noise performance by 0.8 dB can be obtained by increasing the drag by eight counts.

Fig. 7 Multi-objective optimization of the surrogate model: Pareto set found by optimizing the surrogate model and the corresponding allocation of Pareto-optimal solutions in the design space

Figure 8c shows the airfoil shapes from the final Pareto set (Fig. 8b) with a low drag coefficient ($x = [0.0628\,0.4789\,0.080]^T$), i.e., the left-most high-fidelity sample in Fig. 8b, and with a low noise metric ($x = [0.0510\,0.5978\,0.080]^T$), i.e., the right-most high-fidelity sample in Fig. 8b.

5 Conclusion

A computationally efficient procedure for multi-objective optimization of aerodynamic surfaces has been described. The approach exploits a fast surrogate constructed using kriging and space mapping corrected low-fidelity CFD simulation data, as well as the multi-objective evolutionary algorithm that finds a set of designs representing the best trade-offs between design objectives, here, the lift and drag coefficients. A refinement procedure allows for improving the initial Pareto front representation at a low cost depending on the number of high-fidelity verification samples used in the process. The design examples demonstrate a consistent performance of the described method. Future work will extend the approach for higher-dimensional cases, where the initial computational effort related to construction of the response surface approximation model may become a serious issue.
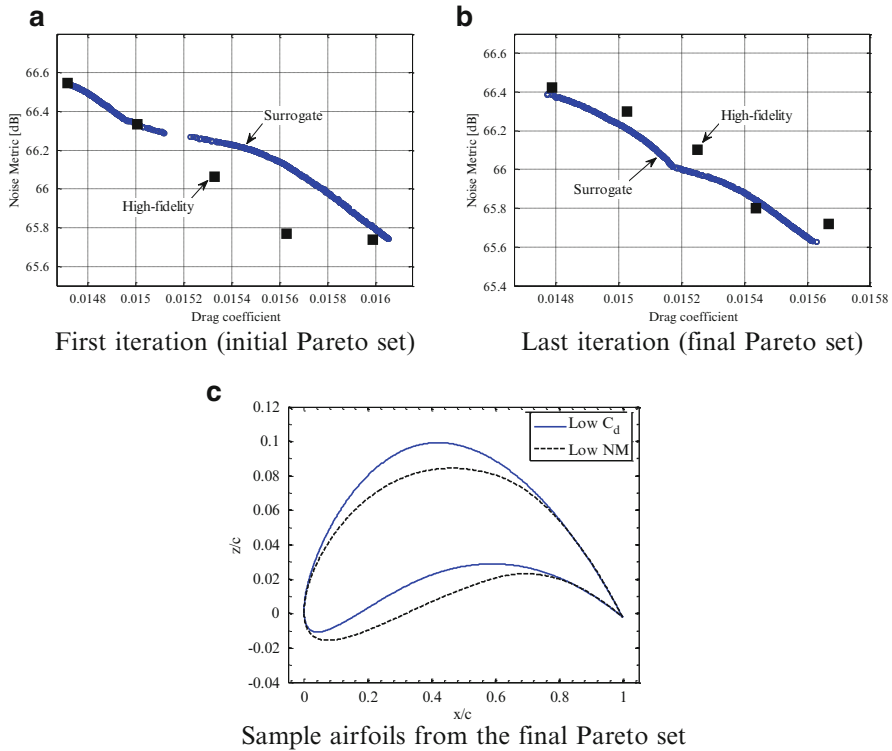
Fig. 8 Pareto front representation obtained by optimizing the surrogate model: (**a**) and (**b**) show surrogate model points (*circles*), and selected high-fidelity model points (*squares*), and (**c**) shows airfoil shapes from the final Pareto set (**b**) for a low drag coefficient and for a low noise metric

References

1. Leoviriyakit, K., Kim, S., Jameson, A.: Viscous aerodynamic shape optimization of wings including planform variables. In: 21st Applied Aerodynamics Conference, Orlando, Florida, 23–26 June 2003
2. Braembussche, R.A.: Numerical optimization for advanced turbomachinery design. In: Thevenin, D., Janiga, G. (eds.) Optimization and Computational Fluid Dynamics, pp. 147–189. Springer, Berlin (2008)
3. Mader, C.A., Martins, J.R.R.A.: Derivatives for time-spectral computational fluid dynamics using an automatic differentiation adjoint. AIAA J. **50**(12), 2809–2819 (2012)
4. Mousavi, A., Nadarajah, S.: Heat transfer optimization of gas turbine blades using an adjoint approach. In: 13th AIAA/ISSMO Multidisciplinary Analysis Optimization Conference, AIAA Paper 2010-9048, Fort Worth, Texas, 13–15 September 2010
5. Leung, T.M., Zingg, D.W.: Aerodynamic shape optimization of wings using a parallel Newton-Krylov approach. AIAA J. **50**(3), 540–550 (2012)
6. Epstein, B., Peigin, S.: Constrained aerodynamic optimization of three-dimensional wings driven by Navier-Stokes computations. AIAA J. **43**(9), 1946–1957 (2005)
7. Nocedal, J., Wright, S.J.: Numerical Optimization. Springer, New York (2006)

8. Kim, S., Hosseini, K., Leoviriyakit, K., Jameson, A.: Enhancement of class of adjoint design methods via optimization of parameters. AIAA J. **48**(6), 1072–1076 (2010)
9. Schmidt, S., Gauger, N., Ilic, C., Schulz, V.: Three dimensional large scale aerodynamic shape optimization based on shape calculus. In: 41st AIAA Fluid Dynamics Conference and Exhibit, AIAA Paper 2011-3718, Honolulu, Hawaii, 27–30 June 2011
10. Queipo, N.V., Haftka, R.T., Shyy, W., Goel, T., Vaidyanathan, R., Tucker, P.K.: Surrogate-based analysis and optimization. Prog. Aerosp. Sci. **41**(1), 1–28 (2005)
11. Forrester, A.I.J., Keane, A.J.: Recent advances in surrogate-based optimization. Prog. Aerosp. Sci. **45**(1–3), 50–79 (2009)
12. Koziel, S., Echeverría-Ciaurri, D., Leifsson, L.: Surrogate-based methods. In: Koziel, S., Yang, X.S. (eds.) Computational Optimization, Methods and Algorithms. Studies in Computational Intelligence, pp. 33–60. Springer, Berlin (2011)
13. Alexandrov, N.M., Lewis, R.M., Gumbert, C.R., Green, L.L., Newman, P.A.: Optimization with variable-fidelity models applied to wing design. In: 38th Aerospace Sciences Meeting & Exhibit, Reno, NV, AIAA Paper 2000-0841, January 2000
14. Robinson, T.D., Eldred, M.S., Willcox, K.E., Haimes, R.: Surrogate-based optimization using multifidelity models with variable parameterization and corrected space mapping. AIAA J. **46**(11), 2814–2822 (2008)
15. Booker, A.J., Dennis Jr., J.E., Frank, P.D., Serafini, D.B., Torczon, V., Trosset, M.W.: A rigorous framework for optimization of expensive functions by surrogates. Struct. Optim. **17**(1), 1–13 (1999)
16. Fonseca, C.M.: Multiobjective genetic algorithms with applications to control engineering problems. Ph.D. thesis, Department of Automatic Control and Systems Engineering, University of Sheffield, Sheffield, UK (1995)
17. Coello Coello, C.A., Lamont, G.B.: Applications of Multi-Objective Evolutionary Algorithms. World Scientific, Singapore (2004)
18. Epstein, B., Peigin, S.: Robust hybrid approach to multiobjective constrained optimization in aerodynamics. AIAA J. **42**(8), 1572–1581 (2004)
19. Nemec, M., Zingg, D.W., Pulliam, T.H.: Multipoint and multi-objective aerodynamic shape optimization. AIAA J. **42**(6), 1057–1065 (2004)
20. Zerbinati, A., Minelli, A., Ghazlane, I., Desideri, J.-A.: Meta-model-assisted MGDA for multi-objective functional optimization. Comput. Fluids, Elsevier **102**(10), 116–130 (2014)
21. March, A., Willcox, W.: Provably convergent multifidelity optimization algorithm not requiring high-fidelity derivatives. AIAA J. **50**(5), 1079–1089 (2012)
22. March, A., Willcox, W.: Constrained multifidelity optimization using model calibration. Struct. Multidiscip. Optim. **46**, 93–109 (2012)
23. Koziel, S., Yang, X.S., Zhang, Q.J. (eds.): Simulation-Driven Design Optimization and Modeling for Microwave Engineering. Imperial College Press, London (2013)
24. Han, Z.-H., Gortz, S., Hain, R.: A variable-fidelity modeling method for aero-loads prediction. Notes Numer. Fluid Mech. Multidiscip. Des. **112**, 17–25 (2010)
25. Han, Z.-H., Gortz, S., Zimmermann, R.: On improving efficiency and accuracy of variable-fidelity surrogate modeling in aero-data for loads context. In: Proceedings of CEAS 2009 European Air and Space Conference, Manchester, UK, 26–29 October 2009, London, UK: Royal Aeronautical Society
26. Han, Z.-H., Zimmermann, R., Gortz, S.: A new cokriging method for variable-fidelity surrogate modeling of aerodynamic data. In: 48th AIAA Aerospace Sciences Meeting Including the New Horizons Forum and Aerospace Exposition, Orlando, FL. AIAA 2010-1225, 4–7 January 2010
27. Koziel, S., Leifsson, L.: Knowledge-based airfoil shape optimization using space mapping. In: 30th AIAA Applied Aerodynamics Conference, New Orleans, Louisiana, 25–28 June 2012
28. Koziel, S., Cheng, Q.S., Bandler, J.W.: Space mapping. IEEE Microw. Mag. **9**(6), 105–122 (2008)
29. ICEM CFD, ver. 14.0, ANSYS Inc., Southpointe, 275 Technology Drive, Canonsburg, PA 15317, 2012.

30. Koziel, S., Leifsson, L.: Surrogate-based aerodynamic shape optimization by variable-resolution models. AIAA J. **51**(1), 94–106 (2013)
31. Leifsson, L., Koziel, S.: Surrogate modeling and optimization using shape-preserving response prediction: a review. Eng. Optim. 1–21 (2015). doi: 10.1080/0305215X.2015.1016509
32. Koziel, S., Leifsson, L: Adaptive response correction for surrogate-based airfoil shape optimization. In: 30th AIAA Applied Aerodynamics Conference, New Orleans, Louisiana, 25–28 June 2012
33. Koziel, S., Leifsson, L: Multi-fidelity airfoil optimization with adaptive response prediction. In: 14th AIAA/ISSMO Multidisciplinary Analysis and Optimization Conference, Indianapolis, Indiana, 17–19 September 2012
34. Eldred, M.S., Giunta, A.A., Collis, S.S.: Second-order corrections for surrogate-based optimization with model hierarchies. In: 10th AIAA/ISSMO Multidisciplinary Analysis and Optimization Conference, Albany, NY, August 30–September 1 2004
35. Abbott, I.H., Von Doenhoff, A.E.: Theory of Wing Sections. Dover Publications, New York (1959)
36. Hosder, S., Schetz, J.A., Mason, W.H., Grossman, B., Haftka, R.T.: Computational-fluid-dynamics-based clean-wing aerodynamic noise model for design. J. Aircr. **47**(3), 754–762 (2010)
37. Menter, F.: Two-equation eddy-viscosity turbulence models for engineering applications. AIAA J. **32**, 1598–1605 (1994)
38. Kinsey, D.W., Barth, T.J.: Description of a hyperbolic grid generation procedure for arbitrary two-dimensional bodies, AFWAL TM 84-191-FIMM, 1984
39. FLUENT, ver. 14.0, ANSYS Inc., Southpointe, 275 Technology Drive, Canonsburg, PA 15317, 2012.
40. Beachkofski, B., Grandhi, R.: Improved distributed hypercube sampling, AIAA Paper 2002-1274. In: 43rd AIAA/ASME/ASCE/AHS/ASC Structures, Structural Dynamics, and Materials Conference, Denver, CO, 22–25 April 2002
41. Bandler, J.W., Cheng, Q.S., Dakroury, S., Mohamed, A.S., Bakr, M.H., Madsen, K., Sondergaard, J.: Space mapping: the state of the art. IEEE Trans. Microwave Theory and Tech. **52**(1), 337–361 (2004)
42. Couckuyt, I.: Forward and inverse surrogate modeling of computationally expensive problems. Ph.D. thesis, Faculty of Engineering and Architecture, Ghent University (2013)